Atmospheric dependence of the direct, diffuse, and global clear-sky conversion ratios between solar photosynthetic active irradiance and photon flux

J. L. Di Laccio[a], P. Russo[a], A. Monetta[a], R. Alonso-Suárez[a,b,*], G. Abal[a,b]

[a] *Laboratorio de Energía Solar, Departamento de Física, CENUR Litoral Norte, UDELAR, Av. L. Batlle Berres km 508, 50000, Salto, Uruguay.*
[b] *Laboratorio de Energía Solar, Instituto de Física, Facultad de Ingeniería, UDELAR, J. Herrera y Reissig 565, 11300, Montevideo, Uruguay.*

Abstract

The ratio of the global solar photosynthetic active radiation (PAR) photon flux (in μmol/m^2 s) to global solar PAR irradiance (in W/m^2) is of interest to convert one into another. This ratio is usually considered as a constant value close to its extraterrestrial value, 4.55 μmol/J. However, this ratio depends on the spectral composition of solar radiation at ground level and it is different for the diffuse and beam components of solar irradiance. Under clear-sky conditions, the three PAR ratios (global, beam and diffuse) are determined by the local atmospheric composition and the relative air mass. In this work, the SMARTS spectral irradiance model with MERRA-2 atmospheric inputs is used to evaluate the dependence of these ratios under clear-sky conditions with air mass, aerosol optical depth (AOD), precipitable water vapor and ozone column. The accuracy of the SMARTS beam spectral irradiance is previously assessed using local spectroradiometer measurements. The clear-sky ratios for the diffuse and direct components increase with increasing air mass, while the global ratio shows only a weak air mass dependence. The clear-sky ratios can be modeled with simple bi-variate linear models in air mass and AOD. These results can be used in similar climatic regions to convert PAR flux to PAR irradiance and vice versa with increased accuracy for the global, direct, and diffuse radiation under cloud-free conditions.

Keywords: PAR irradiance, PAR photon flux, conversion ratios, SMARTS

*Corresponding author: Rodrigo Alonso-Suárez, rodrigoa@fing.edu.uy

1. Introduction

Photosynthetically active radiation (PAR) designates the spectral range of solar radiation from 400-700 nm that most photosynthetic organisms use for living. Knowledge of PAR is important in agriculture and forestry to evaluate biomass production and vegetation growth, and also in oceanography to estimate the euphotic depth, among other applications.

A common method employed in the past for indirectly measuring PAR used broadband global solar irradiance (GHI, G_h) radiometers, which measure the hemispherical global solar irradiance (GHI in W/m^2) in the wavelength range of 285-2800 nm. The PAR flux in W/m^2 was estimated used selective filters to block radiation in the ultraviolet and infrared ranges of the solar spectrum (Escobedo et al., 2006, 2011). In some cases Grossi et al. (2004), the UV contribution (wavelengths below 400 nm) was neglected following an early proposal by Blackburn and Proctor (1983). These indirect methods can provide estimates of the PAR global horizontal irradiance (G_p) in radiometric units (W/m^2). Initial research conducted by Monteith (1972) suggested that horizontal PAR, G_p, was approximately half of GHI and Szeicz (1974) showed that this could be used as a reasonable approximation, regardless of atmospheric aerosol and water vapor concentrations. Currently, moderate-cost commercial PAR quantum sensors are available and indirect methods are seldom used for PAR estimation. These sensors are based on their photovoltaic response to solar irradiance and their output is calibrated in quantum units (μmol/m^2 s) measuring the hemispherical photon flux in the PAR range, (Q_p), usually for a horizontal plane. Most recent work on PAR modeling is based on measurements from PAR quantum sensors (Alados et al., 1996; Tiba and Leal, 2004; Tsubo and Walker, 2007; Denegri, 2016; Foyo-Moreno et al., 2017; Di-Laccio et al., 2021) and some authors work in quantum units (adequate for estimating photosynthetic rates) while others use radiometric units, for compatibility with other solar fluxes.

Both magnitudes (G_p and Q_p) are not proportional. Their ratio depends on the surface solar spectrum, which in turn depends on the local atmospheric composition, the solar radiation optical path and the Sun's apparent position. One of the few studies that deals with this dependence is Akitsu et al. (2015). It uses spectral data for one site in Japan and a radiative transfer model to evaluate Q_p and G_p, and it shows that their ratio can depend on several atmospheric parameters such as water vapor, relative humidity, and cloudiness. However, even under cloudless skies, the problem requires considering the beam and diffuse components of global radiation separately, because these components have different optical paths in the atmosphere and different spectral distributions at ground level. The dependence of the diffuse and global PAR ratios on atmospheric composition (including clouds) was investigated in Dye (2004) using spectral global and diffuse PAR data from one site in Oklahoma, USA. In this work, the dependence on atmospheric composition of the Q_p/G_p ratios for global PAR irradiance and its beam and diffuse components is considered, mostly under clear sky conditions. Novel and locally adjusted expressions for the conversion ratios in terms of the most relevant atmospheric variables are provided.

1.1. PAR ratios

Global PAR irradiance is calculated from the spectral solar global radiation flux (G_λ, expressed in W/m^2 nm) as

$$G_p = \int_{400\,\mathrm{nm}}^{700\,\mathrm{nm}} G_\lambda \, d\lambda. \tag{1}$$

The corresponding global photon flux is calculated taking into account the energy of each mol of photons of a given wavelength, $E_\lambda = N_A hc/\lambda$, where $N_A = 6.022 \times 10^{23}\,\mathrm{mol}^{-1}$ is Avogadro's number, $h = 6.63 \times 10^{-34}\,\mathrm{J\,s}$ is Planck's constant and $c = 2.998 \times 10^8$ m/s is the speed of light in vacuum. Thus,

$$Q_p = \int_{400\,\mathrm{nm}}^{700\,\mathrm{nm}} (G_\lambda/E_\lambda)\, d\lambda = \frac{1}{N_A hc} \int_{400\,\mathrm{nm}}^{700\,\mathrm{nm}} G_\lambda \, \lambda \, d\lambda, \tag{2}$$

and the global conversion ratio $\kappa = Q_p/G_p$ is proportional to the average wavelength weighted by the solar spectrum in the PAR range,

$$\kappa = \frac{Q_p}{G_p} = \frac{1}{N_A hc} \frac{\int_{400\,\mathrm{nm}}^{700\,\mathrm{nm}} G_\lambda\, \lambda\, d\lambda}{\int_{400\,\mathrm{nm}}^{700\,\mathrm{nm}} G_\lambda\, d\lambda} = \frac{1}{N_A hc} \times \langle\lambda\rangle_p\,. \tag{3}$$

As this expression shows, any interaction that shifts G_λ towards the lower wavelength (blue) part of the PAR spectrum will decrease $\langle\lambda\rangle_p$ and the ratio κ. If the shift is towards the higher wavelength (red) part of the PAR spectrum, it will increase $\langle\lambda\rangle_p$ and the ratio κ. Similar relations hold for the diffuse and beam components of G_λ. The constant factor is $1/N_A hc = 8.3593\,\mu\mathrm{mol/J}\ \mu\mathrm{m}$ and, with λ in µm, the global PAR ratio κ has units of µmol/J.

The solar spectrum at the top of the atmosphere (TOA) has some variability due to small orbital variations, changes in Sun activity among other factors. Its long term average has been standarized for use in practical purposes. Using the ASTM (American Society for Testing and Materials) E-490 standard spectrum[1] in Eq. (3) results in

$$\kappa_0 = 4.55\,\mu\mathrm{mol/J}. \tag{4}$$

The same value is obtained if the Wehrli (1985) standard spectrum is used since both standards are very similar in the PAR region. This value is, strictly speaking, associated with beam irradiance at TOA conditions. Using artificial light sources, early work by McCree estimated values of $\kappa = 4.57\,\mu\mathrm{mol/J}$ for global radiation and $\kappa_d = 4.24\,\mu\mathrm{mol/J}$ for the diffuse component (McCree, 1972). These light sources were intended to broadly represent the typical spectrum of each case, referred to by McCree as sun+sky and blue sky, respectively. To this day, the majority of authors continue to employ a value close to the one in Eq. (4) to convert global PAR irradiance to global PAR photon flux. However, the spectral dependence of the ratio κ and the lower value reported for κ_d, suggest that, even under clear-sky conditions, Eq. (3) should be evaluated separately for each radiation magnitude (global, direct, and diffuse) and any significant air-mass or atmospheric dependence in these ratios should be accounted for.

[1] https://www.nrel.gov/grid/solar-resource/spectra-astm-e490.html

Beam spectral irradiance, $G_{b,\lambda}$, is composed of photons arriving within a solid angle of aperture (half-angle) of 5° centered at the Sun's direction (Blanc et al., 2014), thus including some circumsolar irradiance (forward-scattered photons which arrive close to the beam direction). Most collimated commercial sun radiometers use this aperture angle. The spectral solar irradiance arriving on a horizontal plane from other directions (after undergoing possibly multiple scattering in the atmosphere) is the horizontal diffuse component, $G_{d,\lambda}$. Both components are related to the spectral global horizontal irradiance by (McCartney, 1978),

$$G_\lambda = G_{b,\lambda} \cos\theta_z + G_{d,\lambda}, \tag{5}$$

where θ_z is the Sun's zenith angle (between the Sun-Earth line and the local vertical direction). This angle, or equivalently its complement (the solar altitude), define the optical path of the solar beam in a clear atmosphere through the relative air mass, $m \simeq 1/\cos\theta_z$. For high θ_z, more precise expressions, such as the ones proposed in Young (1994); Kasten and Young (1989) can be used, which take into account the Earth's curvature and include refraction effects at low Sun elevations. The beam (κ_b) and diffuse (κ_d) ratios between photon flux and irradiance are defined in a similar way as the global ratio in Eq. (3) and satisfy

$$Q_{p,b} = \kappa_b \times G_{p,b}, \quad \text{and} \quad Q_{p,d} = \kappa_d \times G_{p,d}. \tag{6}$$

These three ratios are required for adequate PAR irradiance to PAR photon flux conversion and vice versa and their modeling has so far been overlooked in the literature.

The main contribution of this article is to investigate the dependence of these ratios on air mass, water vapor and aerosol optical depth under clear-sky conditions, providing multivariate expressions to model them. Spectral irradiance estimates from SMARTS (Simple Model of the Atmospheric Radiative Transfer of Sunshine) with atmospheric information from the MERRA-2 (Modern-Era Retrospective analysis for Research and Applications) re-analysis database are used to estimate the PAR ratios. The beam spectral component from SMARTS is previously validated against clear-sky ground spectral measurements of $G_{b,\lambda}$ from a collimated spectroradiometer, as described in Section 2. The clear-sky ratio analysis based on SMARTS spectra included in Section 3 is the basis to propose and evaluate several models to better describe this ratios under different atmospheric conditions. A brief discussion of the expected effects of cloudiness is also included. Fig. 1 shows a simplified flowchart diagram illustrating the connections between these steps. The work's main conclusions are summarized in Section 4.

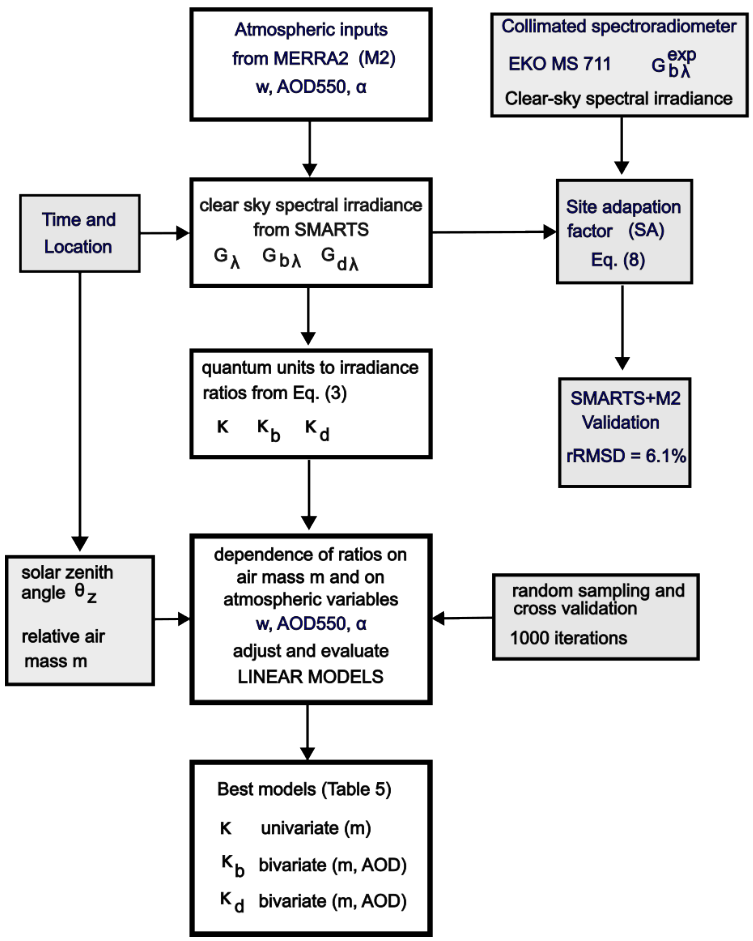

Figure 1: Flowchart illustrating the main steps described in this paper.

2. Validation of SMARTS beam estimates in the PAR range

SMARTS was developed as a simplified model able to match the output from detailed radiative transfer models to within 2% when used with accurate locally measured atmospheric inputs (Gueymard, 2001, 1995). It has been widely used by researchers to establish uniform testing conditions for materials research, optimize day-lighting techniques, and verify broadband radiation models, among other uses in atmospheric science, photo-biology, and health-related physics. It provides estimates for clear-sky spectral horizontal global irradiance in the range 280–4000 nm as well as its beam and diffuse components, among other outputs not used in this work. A recent validation of SMARTS can be found in Gueymard (2019). Updated SMARTS code is freely available in the National Renewable Energy Laboratory website[2] and the publicly available 2.9.5 version has been used for this work.

For the location of this work (in South Eastern South America), a performance analysis of the broadband REST-2 clear-sky model (Gueymard, 2008), which is based on SMARTS parametrizations, has previously been made for the PAR component using MERRA-2 atmospheric inputs (Russo et al., 2022) with good performance. However, the SMARTS spectral estimates have not yet been evaluated in this geographical area. In this section, an assessment for SMARTS beam spectral irradiance in the PAR region (400-700 nm) when used with MERRA-2 atmospheric inputs is reported as a validation, before its use for the estimation of PAR ratios.

2.1. Ground measurements and atmospheric information

A set of 852 ground spectra were measured at the Solar Energy Laboratory in Uruguay (latitude: $-31.2827°$, longitude: $-57.9181°$, altitude: 56 m above mean sea level) for several summer clear-sky days between January 1st and February 11th, 2022. The spectra were recorded at 1-minute intervals using a new EKO beam component MS-711 spectroradiometer with factory calibration

[2] https://www.nrel.gov/grid/solar-resource/smarts.html

(19^{th} March 2020) mounted on a sun tracker EKO STR-22G equipped with a Sun tracking sensor. Auxiliary measurements of broadband global horizontal (G), its beam (G_b) and diffuse (G_d) components and global horizontal PAR irradiance (G_p) were also recorded at 1-min intervals.

Clear-sky samples were selected by visual inspection of the set of broadband measurements. After this selection, 231 records evenly distributed over morning, noon, and afternoon corresponding to four clear days (January 11^{th} and 13^{th} and February 9^{th} and 10^{th}, 2022) were used to evaluate the spectral solar beam estimates from SMARTS.

Table 1: Mean and extreme values of the atmospheric parameters from MERRA-2 and the corresponding SMARTS defaults for STS atmosphere and rural sites.

atmospheric input	minimum	average	maximum	SMARTS default
AOD_{550}	0.047	0.089	0.139	0.0840
w (cm)	1.572	1.800	2.048	4.1252
u_0 (cm)	0.256	0.267	0.273	0.3102

Atmospheric inputs from the re-analysis MERRA2 database[3] (Gelaro et al., 2017) are used in this work. Since there is no close AERONET site, it provides the best information for the region of interest, as discussed in Subsection 2.3. This database provides worldwide atmospheric estimates on a $0.5° \times 0.625°$ grid. Aerosol Optical Depth at 550 nm (AOD_{550} or AOD for short), ozone column (u_o, in cm) and precipitable water vapor (w, in cm) averaged over three-hour periods were used. Mean and extreme values for these variables (simultaneous with the ground measurements) are shown in Table 1 and compared to SMARTS defaults for rural sites and a Sub Tropical Summer (STS) reference atmosphere. Other more stable or non-critical atmospheric parameters were set to their fixed default values: atmospheric pressure was set to 1013.25 hPa, CO_2 concentration to 416.17 ppm[4] and surface albedo to 0.2 (adequate for grassland). The aerosol

[3]https://gmao.gsfc.nasa.gov/reanalysis/MERRA-2/

[4]December 2021 data at Mauna Loa Observatory (https://gml.noaa.gov/ccgg/trends/).

model was set to S&F Rural (Shettle and Fenn, 1979), since the measurement site is in a rural area with mostly clean air and typically low aerosol loads.

2.2. Performance metrics and site adaptation

The usual metrics, MBD (Mean Bias Deviation) and RMSD (Root Mean Squared Deviation) are used to evaluate the performance of the model against the ground measurements, For n measured values (y_i), their corresponding estimates ($\hat{y}_i$) and their residues $\epsilon_i = \hat{y}_i - y_i$, they are defined as MBD $= \frac{1}{n}\sum_{i=1}^{n}\epsilon_i$ and RMSD $= \sqrt{\frac{1}{n}\sum_{i=1}^{n}\epsilon_i^2}$, respectively. In this work, they are expressed in relative form (rMBD and rRMSD) as a percentage of the measurement's average.

These metrics are calculated for each spectral comparison (measured vs. estimated), and the reported values are the average of the 231 selected spectra. The first two rows of Table 2 show the performance indicators for the smoothed spectral beam component[5] from SMARTS in the PAR region (400–700 nm), $\hat{G}_{b,\lambda}$, with without local adaptation with default or MERRA-2 atmospheric inputs. Subestimation predominates in both cases, as seen from the negative rMBD. The overall spectral representation can be seen in Fig. 2.

Table 2: Performance assessment for SMARTS smoothed beam output as compared to the beam PAR spectral irradiance measurements before and after site adaptation. The site adaptation factor from Eq. (7), averaged over all spectra, is indicated. The performance metrics are expressed as a percentage of the average of the measurements, $1364.1\,\mathrm{W\,m^{-2}\,\mu m^{-1}}$.

atmospheric inputs	site-adapted	rMBD (%)	rRMSD (%)
default	no	-9.5	12.2
MERRA-2	no	-10.2	12.4
default	1.1234	0.0	7.0
MERRA-2	1.1338	0.0	6.1

[5]SMARTS includes a post-processing of its beam spectral output with a detector-dependent correction which results in a smoother spectrum and improves the comparison with the experimental values. This is the recommended configuration for the model (Gueymard, 2001).

A simple site adaptation (SA) procedure in the PAR region is used to remove these bias from the spectral estimates. The corrected broadband PAR estimate is matched to its measured counterpart, so that $\hat{G}'_{p,b} = c \times \hat{G}_{p,b} = G_{p,b}$ with a SA factor of

$$c = \frac{G_{p,b}}{\hat{G}_{p,b}} = \frac{\int_{400}^{700} G_{b,\lambda}\, d\lambda}{\int_{400}^{700} \hat{G}_{b,\lambda}\, d\lambda}, \tag{7}$$

with λ in nm. The last two rows in Table 2 show the corresponding SA factors and performance indicators. With the unbiased estimates, SMARTS with MERRA-2 inputs outperforms the default inputs case with a typical deviation of $\simeq 6\%$ of the mean beam spectral irradiance $1364.1\,\mathrm{Wm^{-2}\mu m^{-1}}$. The measured beam spectral irradiance and SMARTS estimates (raw, smoothed, and smoothed-SA) are shown in Fig. 2 for a single event (the PAR region is shaded). The smoothed estimate adjusts well to the measured spectral irradiance before SA in the region 400–450 nm, but it underestimates in the region 450–700 nm. After SA in the PAR region, the underestimation in the 450-700 nm region is mostly resolved at the cost of some overestimation in the 400-550 nm range. There is also an underestimation in the infrared region, which is not relevant for this work.

This general evaluation of the SMARTS beam component suggests that reliable results can be obtained from MERRA-2 atmospheric inputs at this site, particularly if SA is applied. However, it should be emphasized that neither the global spectral irradiance estimate nor its diffuse component have been evaluated, as only beam measured spectra are available in our lab. The lower site-adapted dispersion achieved with MERRA-2 reveals a better spectrum variability representation, a feature relevant for detailed modeling of the PAR ratios. The site-adapted SMARTS estimates with MERRA-2 inputs are used in the following sections. However, it should be emphasized that the ratios, defined in Eq. (3), are independent of the site adaptation factor, so the important takeaway here is that MERRA-2 inputs provide and adequate spectral representation for this site.

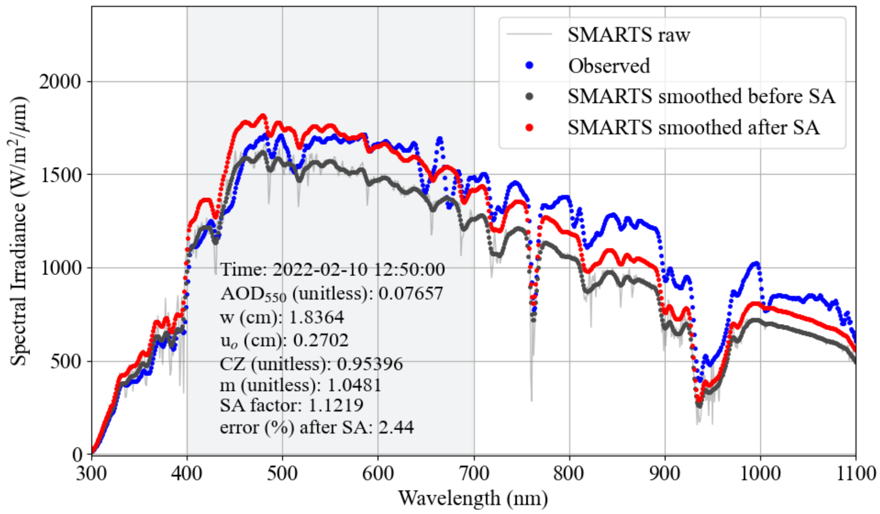

Figure 2: SMARTS raw (gray), smoothed (black) and smoothed SA (red) spectra for a sample instant with MERRA-2 atmospheric inputs. The measured spectrum is shown in blue. The green-shaded background corresponds to the PAR range. Color references are for the web version of the article.

2.3. Comparative performance of different atmospheric databases

There are several worldwide databases providing atmospheric information which is potentially useful for modelling solar irradiance at ground level. The best alternative is to use ground measurements from controlled quality instruments, such as those provided by the AERONET network (Giles et al., 2019). This is a global measurement network initiated by NASA[6], which currently has more than 290 active measuring sites worldwide. Depending on the site, quality-assured (Level 2.0) information, including AOD, Ängstrom exponent and water vapor, can be freely downloaded since 1993 at sub-hour intervals. However, atmospheric composition is local, and when the site of interest is not close to an AERONET (or similar) measuring site, global estimates retrieved from satellite information combined with climate models represent a reasonable choice.

[6] https://aeronet.gsfc.nasa.gov/

Aside from the MERRA-2 re-analysis database, which was introduced in Subsection 2.1 and is used in this work, the CAMS[7] or MODIS databases are two alternatives which have been evaluated (for the target area of this work) against AERONET measurements in the region. The CAMS provides an atmospheric re-analysis based on satellite information and the ECMWF (European Centre for Medium range Weather Forecasts) model with 3-hour resolution over a $0.5° \times 0.5°$ global grid (Inness et al., 2019). The MODIS[8] instrument (MODerate resolution Image Spectroradiometer). on-board the Aqua and Terra Low Earth Orbit satellites, is part of NASA's EOS (Earth Observing System). This project provides[9] daily estimates of atmospheric variables (Wei et al., 2018) over a $1° \times 1°$ global grid since the year 2000.

For AOD550, a comprehensive worldwide validation (Gueymard and Yang, 2020) has been done comparing MERRA2 and CAMS estimates with 15 years of AERONET measurements over 793 sites. Since a climate dependence is recognized, the results are aggregated by climate zone using the updated Köppen-Geiger scheme (Peel et al., 2007). For the Cfa (Warm Temperate) zone, using 172 sites worldwide, they report (in AOD units) an RMSD of 0.098 for MERRA2 and 0.107 for CAMS, respectively. Globally, they also find a better performance for MERRA2. This study is centered on Aerosol products, but it confirms that the choice of the best atmospheric database is a local problem. The MODIS products for AOD and water vapor where evaluated worldwide in Bright and Gueymard (2019b,a) with an aggregation by (broad) climate zone. The RMSD's corresponding to the Warm Temperate zone are listed in Table 3. A local evaluation of the MERRA2 (Laguarda and Abal, 2020) and MODIS (Laguarda, 2021) products for AOD550 and water vapor was recently done using the three

Variable	Region	MERRA2	CAMS	MODIS	Citation
AOD550	Cfa (ww)	0.098	0.107	–	Gueymard and Yang (2020)
AOD550	Cfa (loc)	0.023	–	0.029	Laguarda and Abal (2020)
AOD550	C (ww)	–	–	0.126	Bright and Gueymard (2019a)
AOD550	South America	–	–	0.070	Wei et al. (2019)
w (cm)	C (ww)	–	–	0.504	Bright and Gueymard (2019b)
w (cm)	Cfa (loc)	0.174	–	–	Laguarda and Abal (2020)

Table 3: Evaluations of atmospheric information databases aggregated by climate zone or continent. Only the RMSD performance indicator is shown. In the Region column, (ww) means Aeronet sites worldwide and (loc) means that the three closest Aeronet sites that were used in previous evaluations. The letter C refers to the warm temperate climate zone in the updated Köppen-Geiger scheme (Peel et al., 2007). The MODIS product is daily and obtained from an average of the Terra and Aqua estimates.

closest AERONET sites available in 2019 in the region[10].

Comparisons between the results listed in Table 3 are not straight-forward, because the data is either local or aggregated according to broad climate regions or by geography (continents), depending on the authors. The results from the local studies (Laguarda and Abal, 2020; Laguarda, 2021) show that, when close Aeronet measurements are not available, MERRA2 is a reliable source of atmospheric information for water vapor, AOD and also the Angström exponent (not shown in Table 3) for the target region of this work. For instance, the average AOD550 in Laguarda and Abal (2020) was 0.070 and the rRMSD is 33.4%, a value which is smaller than those reported in the other evaluations for temperate climates Cfa (Gueymard and Yang, 2020) and C (Bright and Gueymard, 2019a). However, for other regions other databases may provide better results.

[7] Copernicus Atmospheric Monitoring System.

[8] https://modis.gsfc.nasa.gov/about/

[9] https://giovanni.gsfc.nasa.gov/giovanni/

[10] A new AERONET site was setup at Montevideo in 2021, 500 km from our target site. It is located $\simeq$ 250 m from the coast in a populated city, hence not representative of the Pampa Humeda suburban areas.

3. Clear-sky PAR ratios analysis

3.1. Air mass dependence

When the photon flux to irradiance ratios are evaluated for each radiation magnitude using SMARTS spectra simultaneous with our measurements in Eq. (3), the averaged results of Table 4 are obtained. The global ratio is, as expected, close to $\kappa_0 = 4.55$ and it shows a weak increasing trend with air mass saturating at $m \simeq 4$, as shown in Fig. 3 (note the minimal variation of the y axis scale). Higher aerosol loads lead to higher ratios for the same air mass.

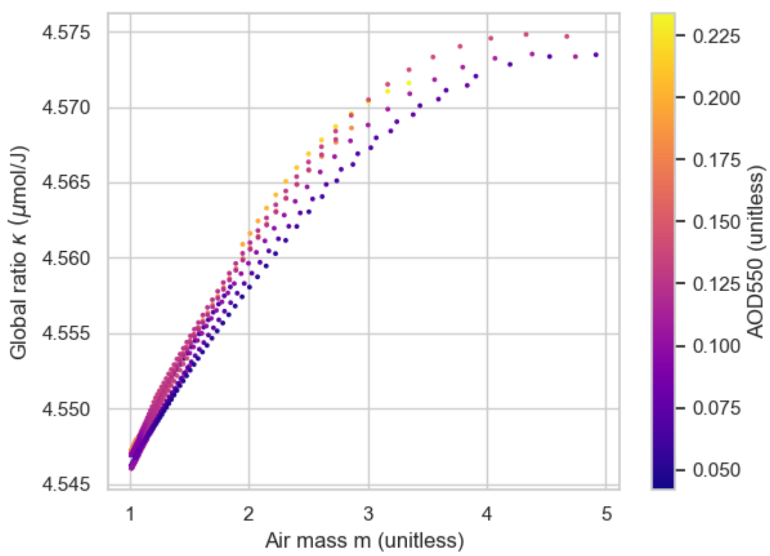

Figure 3: Detailed dependence of the clear-sky global ratio from SMARTS with air mass. Online version: the color scale on the right indicates AOD.

As mentioned in the introduction, Akitsu et al. (2015) model and measure the global PAR ratio, κ, for several sky conditions[11]. The results shown in Fig. 3

[11]This is done using the output of the radiative transfer code Rstar6b (Nakajima and Tanaka, 1986) developed by the Center for Climate System Research at the University of Tokyo.

are consistent with those reported in Fig. 8 of Akitsu et al. (2015) which, for summer and clear-sky conditions in Japan, also observed a small increase of κ with the solar zenith angle. However, as seen in Table 4, the average beam ratio is 1.5% above the global value and the average diffuse ratio is more than 5% below the global value, showing the need to use specific ratios for the different PAR components. A diffuse ratio lower than the global ratio is consistent with the early indirect estimates reported in McCree (1972). The average beam ratio obtained from the measured spectra is shown in the last row of Table 4. This value differs by 0.6% from the corresponding SMARTS estimate, and both beam ratios are higher than the global ratio.

Table 4: Average values for the κ ratios from SMARTS (all air masses) in μmol/J. The last row includes the experimental value for the beam component, for completeness. The standard deviation is expressed as a percentage of the corresponding mean value.

ratio	magnitude	mean	std. dev. (%)	range
$\kappa = Q_p/G_p$	global	4.55	0.15	4.54 – 4.57
$\kappa_b = Q_{p,b}/G_{p,b}$	beam	4.62	0.81	4.59 – 4.81
$\kappa_d = Q_{p,d}/G_{p,d}$	diffuse	4.30	0.82	4.24 – 4.43
κ_b^{exp} (measured)	beam	4.65	0.71	4.62 – 4.81

The air mass dependence of the three ratios for air masses between 1 and 5 is shown in Fig. 4 (the colorscale used in this figure indicates aerosol load). The three ratios increase with air mass, but the diffuse and beam ratios increase at larger rates than the global ratio, leading to variations between 2% and 4% from their $m = 1$ values in the limited range of air masses considered here while the global ratio increases less than 1%. The same behavior is observed for AOD, which has a greater impact on κ_d and κ_b, in that order, and a slight impact on κ. In all cases, AOD tends to increase the ratios. To analyze these different behaviors it must be noted that the three ratios are not independent. From Eqs. (3) and (5) the following relation between the three ratios can be derived,

$$\kappa = \kappa_b \ (1 - f_{pd}) + \kappa_d \ f_{pd}, \tag{8}$$

where f_{pd} is the PAR diffuse fraction, defined in terms of diffuse and global spectral irradiances as

$$f_{pd} = \frac{G_{pd}}{G_p} = \frac{\int_{400\,nm}^{700\,nm} G_{d,\lambda}\, d\lambda}{\int_{400\,nm}^{700\,nm} G_{\lambda}\, d\lambda}. \tag{9}$$

The diffuse fraction (unitless) varies between ~ 0.10 (for clear-sky and a clean dry atmosphere) and can reach 1 under fully cloudy skies (no beam irradiance). This variable is a convenient way to express complex atmospheric effects in a compact form.

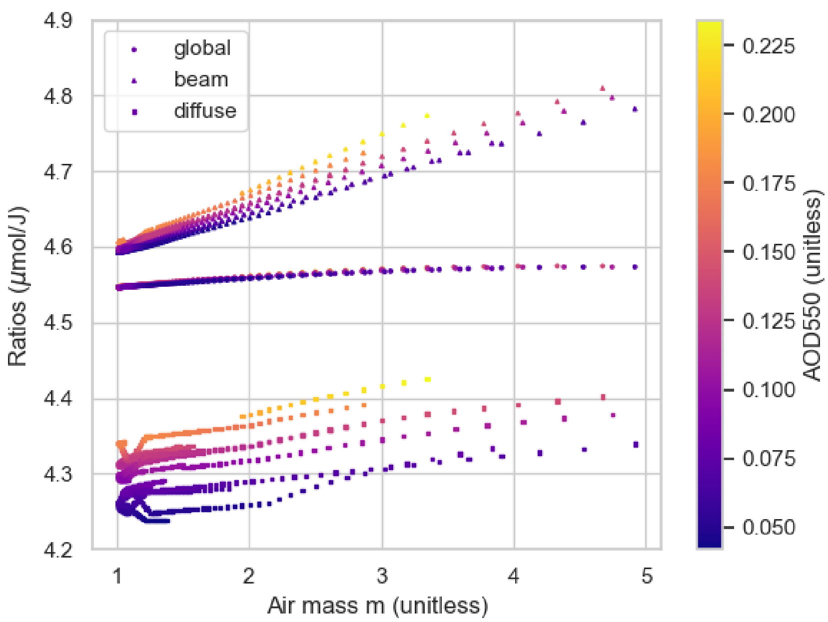

Figure 4: Dependence of the different Q_p/G_p ratios with air mass, as predicted by SMARTS with MERRA2 inputs. Online version: the color scale on the right indicates AOD.

The global ratio is then a weighted average of the beam and diffuse ratios, with the PAR diffuse fraction as weighting factor. Since the clear-sky PAR diffuse fraction increases linearly with air mass, as shown in Fig. 5a, Eq. (8) implies a global ratio $\hat{\kappa}$ with weak air mass dependence, as shown in Fig. 5b. This relation explains the slope change as a function of the air mass and also the dispersion reduction (which is clearly seen in Fig. 4, in other words, the variability from each main trend). The verification of the previous is shown in Fig. 5b, by calculating independently κ_b, κ_d, and f_{pd} from SMARTS spectral estimates and using Eq. (8). This also shows the consistency exhibited by this clear-sky spectral model.

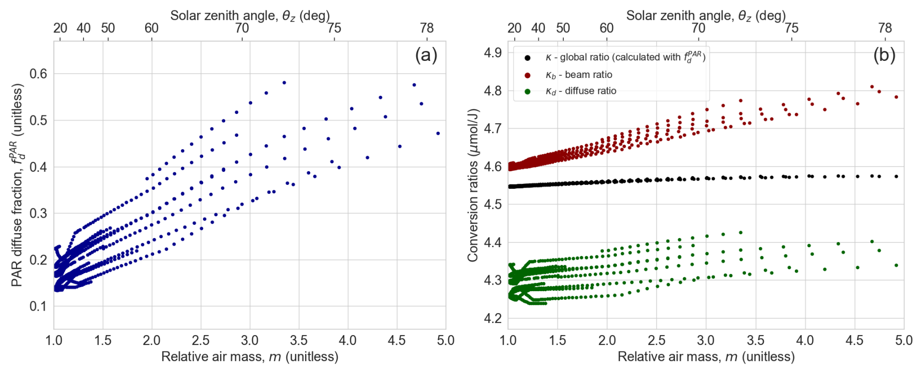

Figure 5: Verification of Eq. (8) by using the SMARTS clear-sky spectral estimates for the beam and diffuse PAR ratios and f_{pd}. (a) PAR diffuse fraction f_{pd} vs m. (b) SMARTS estimates for κ_d and κ_b with the global ratio calculated from Eq. (8).

3.2. Effects of atmospheric composition

As seen in Fig. 4, the air mass is insufficient to explain the complete variability observed in the beam and diffuse ratios. The dispersion around the general air mass trend under clear skies is due to the variability of the relevant atmospheric components, namely, AOD, water vapor, and Ozone. In Fig. 6 the ratios are plotted against each atmospheric variable for $m \leq 2$, as larger values of m produce spikes in the plots that complicates the visualization. κ_b and κ_d have a noticeable variation with AOD, much more marked for the latter. In fact, the AOD inclusion will prove critical (Subsection 3.3) for κ_d modeling. The AOD relevance for modeling κ_b is only for high AOD values. There is also a dependence on w in κ_d, although it is less marked compared to the AOD dependence. Including w in the modeling of κ_d will result in a second-order improvement compared to AOD. Additionally, there is no evident trend between any ratio and ozone column, and water vapor does not impact the global and beam ratios.

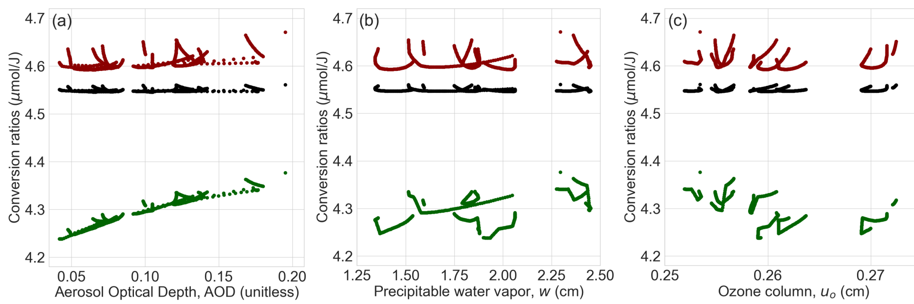

Figure 6: Ratios dependence with atmospheric variables. Color code is the same as in Fig. 4: global ratio (black), beam ratio (dark red), and diffuse ratio (dark green). Dependence with AOD_{550} (a), w (b), and ozone (c). Values with $m \leq 2$ are removed for better visualization.

Cloudiness

This work is based on spectral irradiance from a clear sky model supplemented with measured beam spectral irradiance under mostly clear-sky conditions. These measurements are unreliable when looking for effects of cloudiness, because the beam irradiance is colimated and the signal to noise ratio becomes very small in the presence of clouds. The effects of cloudiness can best be seen in the spectral composition of diffuse irradiance. However, we can show the consistency of our clear-sky results with known results under all-sky conditions, and provide a first modeling extension to the 1-minute (intra-day) time scale.

The effects of cloudiness on PAR diffuse ratios have been considered previously in Dye (2004) using data for diffuse and global spectral irradiance, registered at ground level in one site (Oklahoma USA, latitude 36.6° North). Based on this data, a general relationship between the diffuse and global PAR ratios and the *daily* PAR diffuse fraction, F_{pd}, is established. However, in this work a

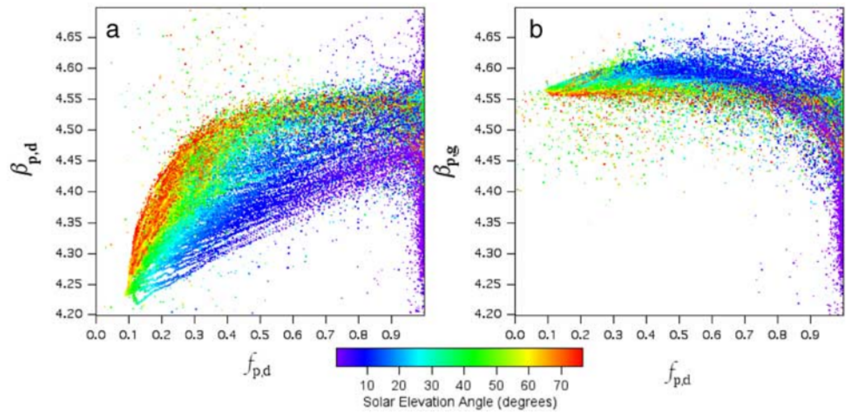

Figure 7: (a) Diffuse and (b) global measured ratios (κ_d and κ in the notation of this paper) as a function on quantum PAR diffuse fraction, as defined in Eq. (10). Color (web version) indicates the solar elevation angle. Reproduced from Dye (2004).

quantum version of the diffuse fraction is used,

$$f_{pd}^{q} = \frac{Q_{pd}}{Q_p} = \frac{\int_{400\,nm}^{700\,nm} G_{d,\lambda}\,\lambda\,d\lambda}{\int_{400\,nm}^{700\,nm} G_{\lambda}\,\lambda\,d\lambda} = \frac{\kappa_d}{\kappa} \times f_{pd}. \tag{10}$$

The relation with f_{pd} follows from Eq. (9) and the definition of the ratios. For clear-sky conditions, this diffuse fraction is linearly related to its version in terms of irradiance, Eq. (9), as checked by the authors. The results in Dye (2004) are expressed in terms of a daily version of the quantum diffuse fraction, F_{pd}^{Q}. For mostly cloudy days $F_{pd}^{Q} \to 1$ and κ is found to decrease linearly from its clear-sky value while κ_d increases non-linearly from its clear-sky value to converge with κ at $F_{pd}^{Q} = 1$, as expected. When expressed in terms of instantaneous measurements, the situation is similar but more variables are involved, as Fig. 7 (reproduced from Dye (2004)) shows. There is a clear increasing trend for κ_d with cloudiness and a much smaller decreasing trend in κ with cloudiness. The dependence of the ratios on air mass, atmospheric components and cloudiness masks these trends as $f_{pd} \to 1$. In particular, for fully cloudy conditions ($f_{pd} = 1$) a high spread is found in the values of both ratios.

However, if focus is made on low air mass conditions (i.e. high elevation angles, yellow and red dots in Fig. 7) a clear trend emerges in both cases. These low air mass trends bound the other measured ratios from below (global) and from above (diffuse). Inspired by Dye (2004), a linear relation may be proposed for the dependence of the κ lower boundary with f_{pd} and a non-linear one for the upper boundary on κ_d,

$$\kappa = a + b\, f_{pd}, \qquad \kappa_d = \frac{c\, f_{pd}}{d + f_{pd}}. \tag{11}$$

The parameters can be obtained from the extreme conditions at low and high f_{pd}. Under extraterrestrial conditions, there are no effects from the atmosphere and no diffuse irradiance, so $\kappa = \kappa_0 = 4.55\,\mu$mol/J, Eq. (4), as $f_{pd} \to 0$. On the other hand, under full cloudiness $f_{pd} \to 1$, all irradiance is diffuse and the global and diffuse ratios must converge, $\kappa_d \to \kappa$, as shown in (Dye, 2004, Fig. 7, for the daily case). The specific ratio at which $\kappa = \kappa_d$ can be read (approximately) from Fig. 7(b) as $\kappa_{d,max} \simeq 4.52\,\mu\text{mol/J}$. Finally, from our clear sky-estimates, Fig. 4, for $f_{pd,min} = 0.1393$ the observed diffuse ratio is $\kappa_{d,min} = 4.25\,\mu\text{mol/J}$. With these boundaries, the coefficients in Eq. (11) are

$$\begin{aligned}
a &= \kappa_0 = 4.55\,\mu\text{mol/J} \\
b &= \kappa_{d,max} - \kappa_0 = -0.03\,\mu\text{mol/J} \\
d &= \frac{\kappa_{d,max} - \kappa_{d,min}}{\kappa_{d,min} \times f_{pd,min}^{-1} - \kappa_{d,max}} = 0.0104 \quad \text{(dimensionless)} \\
c &= \kappa_{d,max}(d+1) = 4.57\,\mu\text{mol/J}
\end{aligned} \tag{12}$$

These general low air mass trends are shown in Fig. 8, with the clear-sky estimates from SMARTS. They bound the global ratios from below and the diffuse ratios from above, as expected. These is a good consistency check for the SMARTS clear-sky ratios as compared with the measured all-sky data from Dye (2004).

A simplified version of the physics can be seen as a balance between complex interactions taking place between the spectrally selective absorption and scattering processes and those which are not spectrally selective, as explained in Dye (2004). According to Eq. (3), the PAR ratios behave essentially as spectrally

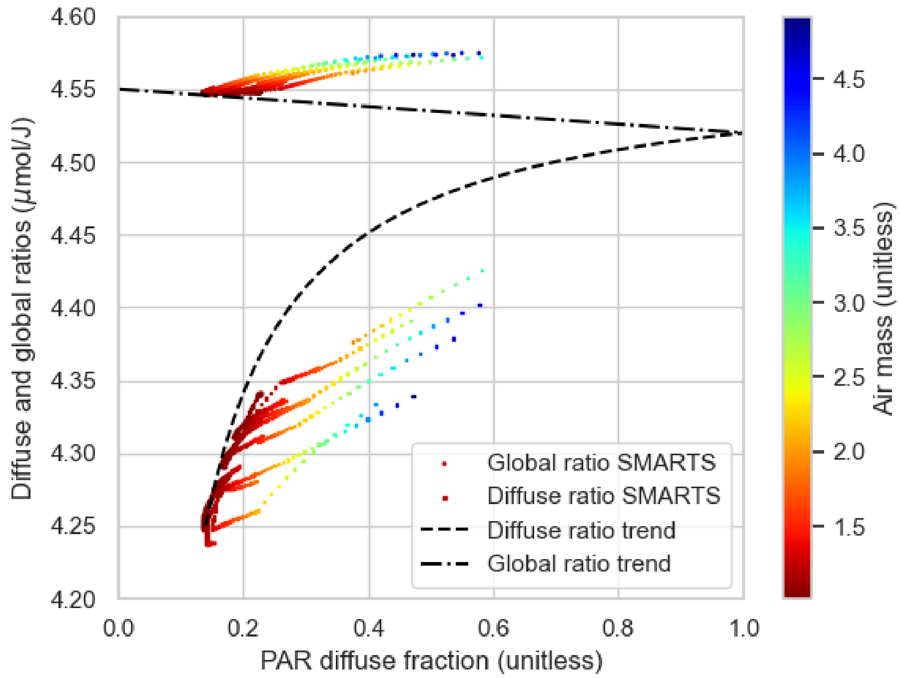

Figure 8: The clear-sky diffuse and global PAR ratios from SMARTS as a function of PAR diffuse fraction, Eq. (9). SMARTS estimates are color coded by air mass using a color map consistent with that in Fig. 7 (low air mass corresponds to high solar elevation). In black, the expected trend of the bounds for these ratios in the presence of cloudiness, according to Eq. (11) and Eq. (13).

weighted average wavelengths. Under clear skies, spectrally selective scatter processes such as molecular (Rayleigh) and fine aerosol scattering dominate and the incident hemispheric diffuse irradiance spectrum reaching the ground is shifted to higher wavelengths (blue), thus $\langle\lambda\rangle$ decreases and so does κ_d as clear-sky conditions are approached. Scattered clouds introduce non-selective scattering processes which tend to preserve the incident beam spectrum, shifting the diffuse spectrum towards higher wavelengths relative to clear-sky conditions which result from mostly selective scattering. This increases $\langle\lambda\rangle$ and also κ_d. The transition takes place gradually as f_{pd} increases from clear-sky values. Under heavy cloud cover, selective absorption and multiple scattering processes complicate the effect on the diffuse spectrum, but in the absence of Rayleigh scattering the shift to longer wavelengths continues until all irradiance is diffuse and $\kappa_d = \kappa$. The spectral effects of scattering are much smaller on global irradiance (under low air masses), since short wavelength photons scattered from beam irradiance appear as diffuse and are still part of the global irradiance. Thus, κ remains rather stable under low air mass, clear-sky conditions. As clouds appear, selective absorption (water vapor and droplets) and multiple scattering processes have the effect of reducing long wavelength components in the global spectrum[12] and $\langle\lambda\rangle$ decreases gradually as $f_{dp} \to 1$.

These general ideas are reasonable starting points but outside the scope of this work. Further research is required to fully understand the spectral effects of the light-atmosphere interactions in the presence of clouds. The parameterization of Eqs. (11) and (12) can be used intra-day for low air mass conditions and range across different sky conditions based on the PAR diffuse fraction.

3.3. Ratios modeling

The ratios' variation with air mass can be parametrized using the polynomial models described in Table 5. The air mass dependence of the beam and diffuse ratios results in a poor fit as measured by R^2 (coefficient of determination), especially in the diffuse case for which $R^2 = 0.251$. When the aerosol load (estimated by AOD_{550} from MERRA-2) is considered the bi-variate models shown in the middle three rows of Table 5 result. The fit for the diffuse ratio improves to $R^2 = 0.976$ and for the direct ratio to $R^2 = 0.992$. The improvement obtained for κ_d by considering AOD is remarkable.

As discussed in Subsection 2.3, the high uncertainties in AOD from reanalysis databases may affect the accurate modelling of solar irradiance broad band diffuse and beam components, while impacting less in the global irradi-

[12]This small shift in the global PAR spectrum was quantified in Fig. 4 of Dye (2004) as a function of cloudiness.

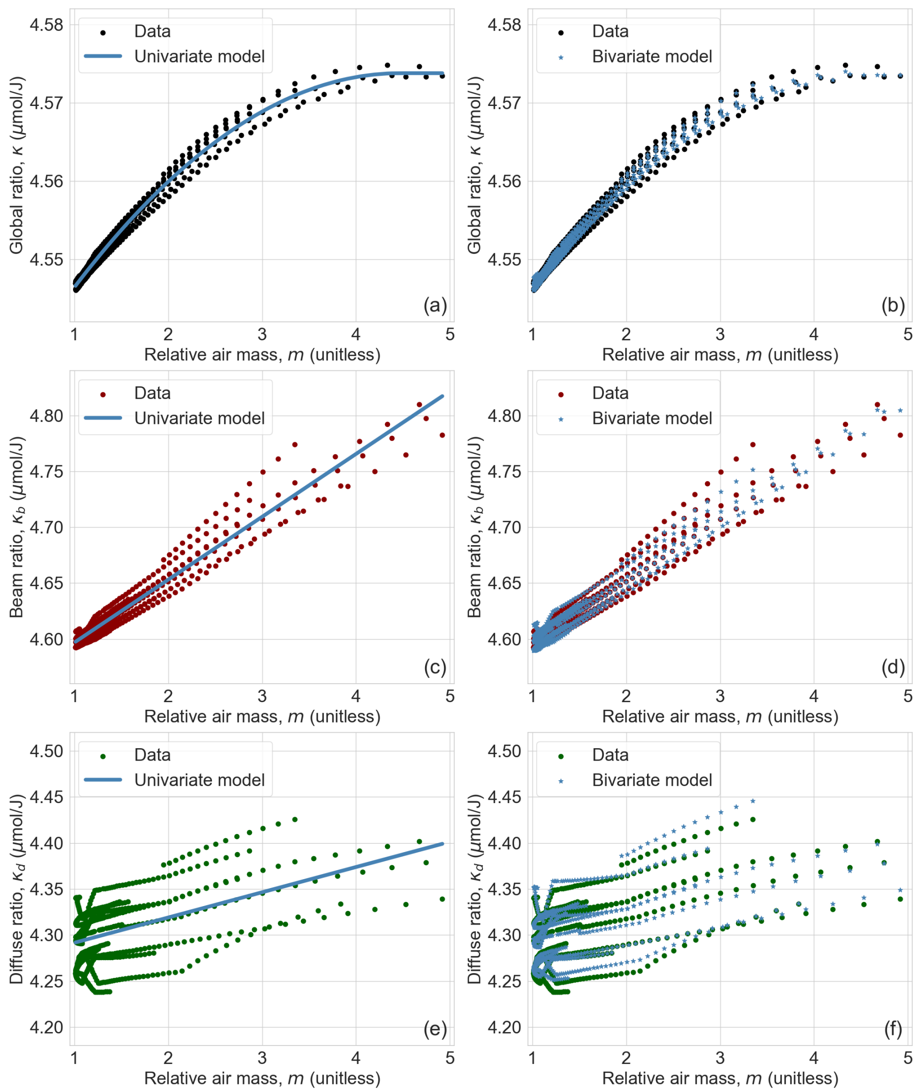

Figure 9: Behaviour of the linear models as a function of the air mass. Models for κ: univariate (a) and bivariate (b). Models for κ_b: univariate (c) and bivariate (d). Models for κ_d: univariate (e) and bivariate (f).

ance. REST2 model (Gueymard, 2008) is a broadband clear-sky model which shares several parametrizations with SMARTS (as both where developed by the same author). A sensitivity analysis for several atmospheric variables used in REST2 has been done in Laguarda and Abal (2020) for the target region of this work. Uncertainties in AOD (or equivalentely β, the Angström parameter) had the largest impact on the broadband beam estimates (DNI). For instance, with a typical uncertainty in AOD550 of 33%, variations in AOD of up to twice this value (66%) caused a 10% change in modelled DNI with only a 2% change in GHI. Increased AOD attenuates the solar beam due to selective scattering while increasing the diffuse component. These broadband results imply that AOD uncertainty may have more impact on the separation of global spectral irradiance into its diffuse and beam components, than on the global estimate itself. The dependence of the three ratios with the atmospheric variables, as seen in Fig. 6, confirms that under clear-skies the largest impact is for AOD on the diffuse ratio κ_d. However, a specific sensitivity analysis for the impact of atmospheric data on the spectral SMARTS outputs is pending.

Table 5: Univariate and bi-variate models for the κ ratios. The relative performance indicators are expressed as percentage of the mean ratios shown in Table 4.

ratio	univariate model	rMBD	rRMSD	R^2
global	$\kappa = -0.00227\,m^2 + 0.0203\,m + 4.5284$	0.00	0.02	0.989
beam	$\kappa_b = 0.0562\,m + 4.5407$	0.00	0.18	0.951
diffuse	$\kappa_d = 0.0274\,m + 4.2643$	0.00	0.71	0.251
ratio	bi-variate model	rMBD	rRMSD	R^2
global	$\kappa = -0.00219\,m^2 + 0.0198\,m + 0.013\,\text{AOD} + 4.5275$	0.00	0.01	0.994
beam	$\kappa_b = 0.0545\,m + 0.199\,\text{AOD} + 4.5225$	0.00	0.07	0.992
diffuse	$\kappa_d = 0.0206\,m + 0.788\,\text{AOD} + 4.1921$	0.00	0.13	0.976
ratio	tri-variate model	rMBD	rRMSD	R^2
diffuse	$\kappa_d = 0.0200\,m + 0.814\,\text{AOD} - 0.006\,w + 4.2018$	0.00	0.12	0.979

The models adjustment and validation was done using a standard cross-validation procedure in which the data set is randomly split into two halves for training and evaluation. This procedure is repeated independently 1000 times to ensure the repeatability of the results. The univariate model is satisfactory for the global ratio, being only slightly improved by the inclusion of AOD. Requiring AOD data access increases the complexity the model's implementation as compared to only requiring m, which results from a simple calculation of the apparent solar position. For completeness, a tri-variate model for κ_b including w is reported in the last row of Table 5, although the performance gain by including this second atmospheric variable is marginal.

The univariate and bi-variate estimates are shown in Fig. 9 along with the simulated ratios. A fair modeling of the global ratio requires at least a second-order polynomial in m. Polynomial parametrizations should not be extrapolated outside their fitting range. They may also introduce artifacts in the range's borders. Due to these issues, the models for the global ratio in Table 5 are maintained constant for $m \geq 4.5$, allowing their safe utilization for $\theta_z \geq 78°$. In the case of the bi-variate model, the average AOD value (AOD = 0.1) is used (and recommended) to complete the model for $m \geq 4.5$. Ozone does not play a relevant role in the PAR range. Fig. 10 illustrates the residuals of the univariate, bi-variate, and tri-variate κ_d models in relation to w and u_0. It is evident that there is a significant reduction in residuals when transitioning from the univariate to the bi-variate model, which includes AOD. However, beyond the bi-variate model, the tri-variate model only marginally improves the residuals. It is noticeable that after including AOD, the residuals exhibit no correlation with w and u_0, indicating their limited additional explanatory power.

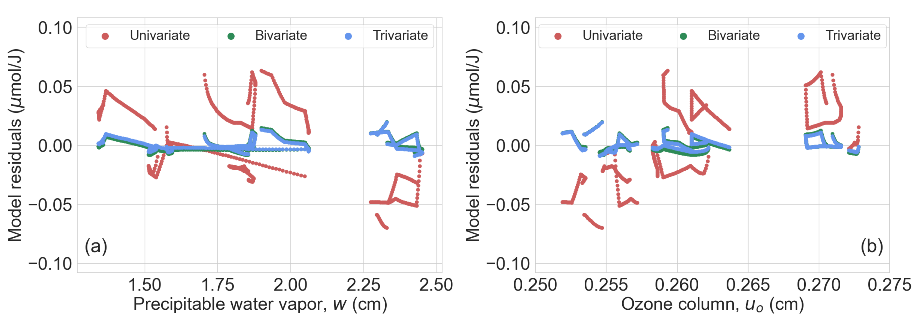

Figure 10: Residuals of the κ_d ratio modeling. Dependence with w (a) and u_0 (b).

These models have been trained using SMARTS clear-sky estimates for the target region (latitude 30° South, rural site) with low aerosol loads and low elevation in the Pampa Húmeda of South eastern South America. This region is classified as Cfa (temperate with warm summer) in the Köppen-Geiger updated climate classification scheme (Peel et al., 2007). These models describe the spectral effects of scattering and absorption in terms of the PAR ratios. They can be used safely for similar climatic regions but for best results, the coefficients should be locally adjusted for different climates or sites with high altitudes or aerosol loads.

4. Conclusions

The spectral outputs for global irradiance (and its beam and diffuse components) from clear-sky SMARTS model have been used to explore the dependence of the PAR photon flux to irradiance ratios with air mass and other atmospheric components. An assessment of the spectral beam component of SMARTS with MERRA2 atmospheric inputs was performed against clear-sky ground spectral measurements. A simple simple site adaptation procedure can considerably improve the estimates in the PAR region, which are otherwise affected by a significant negative bias. The use of MERRA-2 atmospheric information results in a better spectral representation (with respect to the default atmospheric values) with typical deviations of 6% of the mean spectral irradiance, after bias correction.

The global PAR photon flux to irradiance ratio is only weakly dependent on the air mass under clear-sky conditions, for the air mass range considered in this work (between 1 and 5). In the same range, the corresponding diffuse and beam ratios increase with air mass 2% and 4% respectively. The relation between the three ratios and the PAR diffuse fraction is found from theoretical considerations.

The air mass is not the only variable affecting the diffuse and beam PAR conversion ratios. Aerosol load or AOD is required for an adequate representation of the diffuse PAR conversion ratio. A bi-variate linear model including both variables adequately represents the diffuse and beam ratios variations. On the other hand, a univariate linear model in air mass is sufficient for modeling the global PAR ratio. Cloudiness effects are briefly discussed, and the clear-sky diffuse and global ratios as functions of diffuse fraction are shown to be consistent with the expected upper and lower bounds resulting from low air mass (or high solar elevation) conditions. This enables an initial intra-day modeling of the diffuse and global ratios for low air mass and different sky conditions, based on the PAR diffuse fraction.

These simple models can be used in practice to improve the conversion of PAR photon flux measurements to irradiance units in regions with similar climate and geography as the target region in this work. For other regions, the proposed parametrizations are adequate, but a local adjustment of the coefficients may be required for accurate results.

The extraterrestrial (TOA) conversion factor 4.55 µmol/J for the global ratio is adequate for most purposes under clear or cloudy skies. Spectral irradiance data under all-sky conditions for the diffuse spectral component is required to study in more detail the spectral effects of cloudiness on the diffuse-beam separation. At high cloudiness conditions, the diffuse ratio becomes identical with the global ratio, as reported by Akitsu et al. (2015) and Dye (2004). To investigate the detailed dependence of the diffuse and beam PAR ratios as the non-selective scattering due to clouds begins to dominate, is the next natural step in this research program.

Acknowledgments

The authors acknowledge partial financial support from CSIC Research Group Program, Universidad de la República, Uruguay.

References

Akitsu, T., Kume, A., Hirose, Y., Ijima, O., M., N.K., 2015. On the stability of radiometric ratios of photosynthetically active radiation to global solar radiation in Tsukuba, Japan. Agricultural and Forest Meteorology 209-210, 59–68.

Alados, I., Foyo-Moreno, I., Alados-Arboledas, L., 1996. Photosynthetically active radiation: measurements and modelling. Agricultural and Forest Meteorology 78, 121–131. doi:https://doi.org/10.1016/0168-1923(95)02245-7.

Blackburn, W.J., Proctor, J.T.A., 1983. Estimating photosynthetically active radiation from measured solar irradiance. Solar Energy 31, 233–234. doi:10.1016/0038-092X(83)90087-7.

Blanc, P., Espinar, B., Geuder, N., Gueymard, C., Meyer, R., Pitz-Paal, R., Reinhardt, B., Renné, D., Sengupta, M., Wald, L., Wilbert, S., 2014. Direct normal irradiance related definitions and applications: The circumsolar issue. Solar Energy 110, 561–577. doi:https://doi.org/10.1016/j.solener.2014.10.001.

Bright, J., Gueymard, C., 2019a. Climate-specific and global validation of modis aqua and terra aerosol optical depth at 452 aeronet stations. Solar Energy 183, 594–605. doi:10.1016/j.solener.2019.03.043.

Bright, J.M., Gueymard, C.A., 2019b. Climate-specific and global validation of MODIS Aqua and Terra aerosol optical depth at 452 AERONET stations. Solar Energy 183, 594–605. doi:https://doi.org/10.1016/j.solener.2019.03.043.

Denegri, M., 2016. Radiación Fotosintéticamente Activa en Luján, Buenos Aires. estimación en función de la irradiación solar global. XVI Reunión Argentina y VIII Latinoamericana de Agrometeorología. Puerto Madryn, Chubut .

Di-Laccio, J., Alonso-Suárez, R., Abal, G., 2021. One-minute assessment of photosynthetically active radiation (PAR) models in Uruguay. Proceedings of the ISES Solar World Congress 2021 doi:doi:10.18086/swc.2021.38.01.

Dye, D.G., 2004. Spectral composition and quanta-to-energy ratio of diffuse photosyntetically active radiation under diverse cloud conditions. Journal of Geophysical Research 109. doi:10.1029/2003JD004251.

Escobedo, J., Gomes, E., Oliveira, A.P., Soares, J., 2006. Radiações solares UV, PAR e IV: I - estimativa em função da global. Avances en Energías Renovables y Medio Ambiente 10, 79 – 86.

Escobedo, J., Gomes, E., Oliveira, A.P., Soares, J., 2011. Ratios of UV, PAR and NIR components to global solar radiation measured at Botucatu site in Brazil. Renewable Energy 36, 169 178.

Foyo-Moreno, I., Alados, I., Alados-Arboledas, L., 2017. A new conventional regression model to estimate hourly photosynthetic photon flux density under all sky conditions. Int. J. Climatol 37. doi:DOI:10.1002/joc.5063.

Gelaro, R., McCarty, W., Suârez, M., Todling, R., Molod, A., Takacs, L., Randles, C., Darmenov, A., Bosilovich, M., Reichle, R., Wargan, K., 2017. The modern-era retrospective analysis for research and applications, Version 2 (MERRA-2). Journal of Climate 30, 5419–5454. doi:https://doi.org/10.1175/JCLI-D-16-0758.1.

Giles, D.M., Sinyuk, A., Sorokin, M.G., Schafer, J.S., Smirnov, A., Slutsker, I., Eck, T.F., Holben, B.N., Lewis, J.R., Campbell, J.R., Welton, E.J., Korkin, S.V., Lyapustin, A.I., 2019. Advancements in the aerosol robotic network (aeronet) version 3 database – automated near-real-time quality control algorithm with improved cloud screening for sun photometer aerosol optical depth (aod) measurements. Atmospheric Measurement Techniques 12, 169–209. doi:10.5194/amt-12-169-2019.

Grossi, H., Righini, R., Dursi, O., 2004. Primeras mediciones de la Radiación Fotosintéticamente Activa en San Miguel, Provincia de Buenos Aires. ASADES 8, 13–17.

Gueymard, C., 1995. SMARTS2, Simple Model of the Atmospheric Radiative Transfer of Sunshine: Algorithms and performance assessment. Technical Report Rep. FSEC-PF-270-95,. Florida Solar Energy Center. URL: http://www.fsec.ucf.edu/en/publications/pdf/FSEC-PF-270-95.pdf.

Gueymard, C.A., 2001. Parametrized transmittance model for direct beam and circumsolar spectral irradiance. Solar Energy 71, 325–346.

Gueymard, C.A., 2008. REST2: high-performance solar radiation model for cloudless-sky irradiance, illuminance, and photosynthetically active radiation – validation with a benchmark dataset. Solar Energy 82, 272–285. doi:https://doi.org/10.1016/j.solener.2007.04.008.

Gueymard, C.A., 2019. The SMARTS spectral irradiance model after 25 years: New developments and validation of reference spectra. Solar Energy 187, 233–253.

Gueymard, C.A., Yang, D., 2020. Worldwide validation of cams and merra-2 reanalysis aerosol optical depth products using 15 years of aeronet observations. Atmospheric Environment 225, 117216. doi:https://doi.org/10.1016/j.atmosenv.2019.117216.

Inness, A., Ades, M., Agustí-Panareda, A., Barré, J., Benedictow, A., Blechschmidt, A.M., Dominguez, J.J., Engelen, R., Eskes, H., Flemming, J., Huijnen, V., Jones, L., Kipling, Z., Massart, S., Parrington, M., Peuch, V.H., Razinger, M., Remy, S., Schulz, M., Suttie, M., 2019. The cams reanalysis of atmospheric composition. Atmospheric Chemistry and Physics 19, 3515–3556. doi:10.5194/acp-19-3515-2019.

Kasten, F., Young, A., 1989. Revised optical air mass tables and approximation formula. Applied Optics 28, No. 22, 4735–4738.

Laguarda, A., 2021. Modelado de la irradiancia solar sobre la superficie terrestre. Ph.D. thesis. Facultad de Ingeniería, Universidad de la República, Uruguay. http://les.edu.uy/tesis/PhD_agustin-laguarda.pdf.

Laguarda, A., Abal, G., 2020. Impacto de la incertidumbre de las variables atmosféricas de la base MERRA-2 en el modelado de la irradiancia solar en cielo despejado. Avances en Energías Renovables y Medio Ambiente 24, 212–221. URL: http://les.edu.uy/papers/AVERMA2020_MERRA_evaluation.pdf. iSSN 2314-1433.

McCartney, H.A., 1978. Spectral distribution of solar radiation II: global and diffuse. Quart. J. R. Met. Soc. 104, 911–926.

McCree, K., 1972. Test of current definitions of photosynthetically active radiation against leaf photosynthesis data. Agricultural Meteorology 10, 443–453.

Monteith, J.L., 1972. Productivity in tropical ecosystems. Journal of Applied Ecology 9, 747–766. doi:https://doi.org/10.2307/2401901.

Nakajima, T., Tanaka, M., 1986. Matrix formulations for the transfer of solar radiation in a plane-parallel scattering atmosphere. Journal of Quantitative Spectroscopy and Radiative Transfer 35, 13–21. doi:https://doi.org/10.1016/0022-4073(86)90088-9.

Peel, M., Finlayson, B., Mcmahon, T., 2007. Updated world map of the koppen-geiger climate classification. Hydrology and Earth System Sciences Discussions 4. doi:10.5194/hess-11-1633-2007.

Russo, P., Laguarda, A., Abal, G., Piccioli, I., 2022. Performance of the REST2 model for 1-minute clear-sky solar irradiance with MERRA-2 atmospheric inputs, in: Proceedings of the IX CBENS Congresso Brasileiro de Energia Solar, Florianopolis, Brazil, p. 9.

Shettle, E.P., Fenn, R.W., 1979. Models for the Aerosols of the Lower Atmosphere and the Effects of Humidity Variations on their Optical Properties. Technical Report. Air Force Geophysics Laboratory, USAF. URL: https://www.researchgate.net/publication/235074087_Models_for_the_Aerosols_of_the_Lower_Atmosphere_and_the_Effects_of_Humidity_Variations_on_their_Optical_Properties.

Szeicz, G., 1974. Solar radiation for plant growth. Journal of Applied Ecology 11, 617–636.

Tiba, C., Leal, S.D.S.A., 2004. Medidas e modelagem da radiação PAR para o nordeste do Brasil. 5º Encontro de Energia no Meio Rural e Geração Distribuída. Campinas – São Paulo doi:8.

Tsubo, M., Walker, S., 2007. Relationships between photosynthetically active radiation and clearness index at Bloemfontein, South Africa. Theor. Appl. Climatol. , 17–25.

Wehrli, C., 1985. Extraterrestrial Solar Spectrum. Publication no. 615. Physikalisch-Meteorologisches Observatorium + World Radiation Center.

Wei, J., Li, Z., Peng, Y., Sun, L., 2019. Modis collection 6.1 aerosol optical depth products over land and ocean: validation and comparison. Atmospheric Environment 201, 428–440. doi:https://doi.org/10.1016/j.atmosenv.2018.12.004.

Wei, J., Sun, L., Peng, Y., Wang, L., Zhang, Z., Bilal, M., Ma, Y., 2018. An improved high-spatial-resolution aerosol retrieval algorithm for modis images over land. Journal of Geophysical Research: Atmospheres 123, 12,291–12,307. doi:https://doi.org/10.1029/2017JD027795.

Young, A.T., 1994. Air mass and refraction. Appl. Opt. 33, 1108–1110. URL: https://opg.optica.org/ao/abstract.cfm?URI=ao-33-6-1108, doi:10.1364/AO.33.001108.